TENTH AUSTRALASIAN FLUID MECHANICS
CONFERENCE - UNIVERSITY OF MELBOURNE
11-15 DECEMBER 1989

DIRECT NUMERICAL SIMULATIONS OF THE IMPULSIVE FLOW PAST A WEDGE-LIKE CORNER

C. MAVRIPLIS[1], P. FISCHER[1] and G.E. KARNIADAKIS[2*]

[1]Mechanical Engineering
Massachusetts Institute of Technology, USA

[2]Mechanical and Aerospace Engineering
Princeton University, USA

I. INTRODUCTION

The unsteady, separated flow past a sharp-edged body serves as a model for the mechanism of generation of circulation and the subsequent evolution of a vortex sheet around bodies of aerodynamic interest. The first systematic observations of edge vortex formation dates back to flow visualizations of Prandtl and Tietjens (1904). More recent experiments by Pierce (1961) and Pullin and Perry (1980) have also focused on the visualization of the starting vortex, although in the latter work there is an attempt for more quantitative studies. On the computational side, a number of studies have been undertaken over the past two decades to model the large-scale vortex sheet motion by using a finite number of point vortices for inviscid-type computations (see Krasny (1987) for a review), or by employing a modified vortex method appropriate for viscous simulations (Spalart et al (1984)). Although visual agreement with the experiment for the outer large-scale structure of the rolled-up vortex sheet was obtained in these previous studies, several important details of the flow field, especially in the near-wedge-apex region, were missed. To the best of our knowledge, no accurate computation of these flows has appeared in the literature to date. Several basic fluid dynamics questions associated with these flows remain unanswered. The most puzzling one, perhaps, relates to the extent that the suddenly appeared small-scale undulations of the large-scale vortex sheet, as have been photographed by Pierce (1961) and Pullin and Perry (1980), persist, and what exactly the corresponding instability mechanism might be.

In this work the flow past a wedge-like corner is computed via direct numerical simulation based on conforming and nonconforming spectral element methods (Maday and Patera (1987)). These two different discretization procedures in the context of the current problem illustrate some of the essential features of the spectral element method, and in particular, the flexibility of the method in resolving accurately and efficiently flows in complex, even singular geometries. The current simulation closely follows the experiments of Pullin and Perry (1980) performed at relatively low Reynolds number and for different wedge-angles. The exact geometry consists of a wedge of angle $\beta\pi$ attached to the upper wall of a flat channel; the flow is turned on impulsively at a location upstream of the wedge, and the transient flow response is followed in time. Our objective here is to compare the results of our high-accuracy computation with experimental data and similarity solutions (Pullin (1979)), and also to provide a detailed data base for use in validating vortex-type methods in future development work.

*Address correspondence to G.E.Karniadakis.

In the following, we first review the spectral element methodology and explain the two different discretization procedures. We then present results obtained using the two different approaches and compare with experimental data and results of inviscid similarity solutions; for the comparison both streamline patterns and the relative position of the center of the rolled-up sheet are presented.

2. METHODOLOGY

Our objective is the solution of the time-dependent incompressible Navier-Stokes equations in a two-dimensional domain Ω,

$$\frac{\partial \mathbf{u}}{\partial t} = -\frac{\nabla p}{\rho} + \nu \nabla^2 \mathbf{u} + \mathbf{f} \qquad \text{in } \Omega \tag{1a}$$

$$\nabla \cdot \mathbf{u} = 0 \qquad \text{in } \Omega \tag{1b}$$

where $\mathbf{f}$ includes the nonlinear contributions and any other forcing terms. These equations are advanced in time using an explicit/implicit fractional time-stepping scheme (Karniadakis (1989)), which results in a set of separately solvable equations for the pressure $p(x,y,t)$ and the velocity $\mathbf{u}(x,y,t)$. The nonlinear terms are treated as a simple inhomogeneity appearing in the pressure-velocity elliptic equations. Such a temporal discretization of equations (1) is consistent with the spatial spectral element discretization, where all solvers are constructed on the basis of a hierarchy of nested operators proceeding from the highest (for example elliptic contributions) to the lowest derivatives. This philosophy is motivated by the fact that the highest derivatives in an equation govern the continuity requirements, conditioning, and stability of the system of equations (1). Given the brevity of the current paper we shall limit our discussion to the elliptic equations, an example of which is the Helmholtz equation for the viscous velocity correction,

$$(\nabla^2 - \lambda^2)\phi = g \qquad \text{in } \Omega \tag{2}$$

where g is an inhomogeneity computed from the previous pressure substep and $\lambda^2 = 2/(\nu \Delta t)$ (for a Crank-Nicolson scheme) is a positive constant. In addition, let us assume homogeneous boundary conditions $\phi = 0$ on $\partial\Omega$. We now turn to the discretization of (2) using concepts of conforming and nonconforming spectral element techniques.

2.1 Conforming Spectral Element Methods

Equation (2) can be further discretized using planar spectral elements in the $x_1 - x_2$ plane. If we define H_0^1 as the standard Sobolev space that contains functions which satisfy homogeneous boundary conditions and introduce test-

functions $\psi \in H_0^1$, we can then write the equivalent variational statement of (2) as,

$$\int_\Omega \frac{\partial \psi}{\partial x_j}\frac{\partial \phi}{\partial x_j} d\vec{x} + \lambda^2 \int_\Omega \psi\phi d\vec{x} = -\int_\Omega \psi f d\vec{x}. \qquad (3)$$

The spectral element discretization corresponds to numerical quadrature of the variational form (3) restricted to the space $X_h \subset H_0^1$. The discretization space X_h is defined in terms of the spectral element discretization parameter $h = (K, N_1, N_2)$, where K is the number of subdomains. X_h is then the subspace of H_0^1 consisting of functions that are L^2 over the entire domain Ω and which are tensor products of piecewise high order polynomials of degree less than or equal to N_1 and N_2 in the x_1 and x_2 directions respectively on each subdomain Ω^k. Testing the variational form with respect to testfunctions of X_h and performing all inner products by Gauss-Lobatto numerical quadrature, Equation (3) becomes

$$\sum_{k=1}^{K}\sum_{p=0}^{N_1}\sum_{q=0}^{N_2} \rho_{pq} J_{pq}^k [\frac{\partial \psi_h}{\partial x_j}\frac{\partial \phi_h}{\partial x_j}]_{\xi_{pq}^k} + \lambda^2 \sum_{k=1}^{K}\sum_{p=0}^{N_1}\sum_{q=0}^{N_2} \rho_{pq} J_{pq}^k [\psi_h \phi_h]_{\xi_{pq}^k}$$
$$= -\sum_{k=1}^{K}\sum_{p=0}^{N_1}\sum_{q=0}^{N_2} \rho_{pq} J_{pq}^k [\psi_h f]_{\xi_{pq}^k}, \quad (4)$$

where ξ_{pq}^k are the appropriate Gauss-Lobatto points and $\rho_{pq} = \rho_p \rho_q$ the corresponding weights. J_{pq}^k is the Jacobian of the transformation from global to local coordinates $(x_1, x_2) \Rightarrow (r, s)$, for the two-dimensional element k. The next step in implementing (4) is the selection of a basis which reflects the structure of the piecewise smooth space X_h. We choose an interpolant basis with components defined in terms of Legendre/Chebyshev-Lagrangian interpolants, $h_i(r_j) = \delta_{ij}$. Here, r_j represents local coordinate and δ_{ij} is the Kronecker-delta symbol. It has been shown in Maday and Patera (1987) that such a spectral element implementation converges spectrally fast to the exact solution for a fixed number of elements K and $N \to \infty$, for smooth data and solution, even in non-rectilinear geometries.

Having selected the basis we can proceed in writing the local to element k spectral element approximations for ϕ_h^k,(or ψ_h^k) as follows,

$$\phi_h^k = \phi_{mn}^k h_m(r) h_n(s) \quad \forall m, n \in (0, ..., N_1), (0, ..., N_2), \quad (5)$$

where ϕ_{mn}^k is the local nodal value of ϕ_h. The geometry is also represented via similar type tensorial products with same-order polynomial degree. We then insert (5) into (4) and choose test functions ψ_{mn}, which are non-vanishing at only one global node, to arrive at the discrete matrix system. A typical conforming spectral element mesh for the problem we consider here is shown in Figure 1 consisting of $K = 90$ elements; the nodes corresponding to the Gauss-Lobatto Chebyshev points are not shown here. This mesh was used for the presented results with $N_1 = N_2 = 7$.

2.2 Nonconforming Spectral Element Methods

The nonconforming discretization greatly improves the flexibility of the spectral element approach by allowing arbitrary element matchups in the geometric mesh while preserving the convergence properties of the spectral element discretization.

A nonconforming discretization is one in which the discretization space X_h is not a subset of H_0^1. An additional consistency error associated with the deviation of X_h from H_0^1 is therefore incurred. Unlike other nonconforming methods (see Strang and Fix (1973) and Dorr (1989)), this method is based on the explicit construction of the appropriate nonconforming space of approximation to minimize the consistency error. To define the approximation space X_h, we first introduce a new structure known as the set of mortars γ^p, which are defined as the intersection of adjacent element edges. Upon this structure, Φ is defined as the mortar function, which is a polynomial of degree N in the local one-dimensional mortar variable s. The approximation space is then defined as follows. X_h consists of the functions ϕ in L^2 that are tensor products of polynomials of degrees N_1 and N_2 in the two directions respectively of each element k, such that the two following conditions are satisfied:

1- the vertex condition: at each vertex q of each element,
$$\phi(q) = \Phi(q).$$
2- the L^2 condition: over each elemental edge $\forall \Psi \in P_{N-2}$
$$\int_{edge} (\phi - \Phi)\Psi ds = 0.$$

The vertex condition ensures exact continuity at cross points where the normal derivative has more than one sense. The L^2 condition represents a L^2 minimization of the jump in functions with orthogonality to $N-2$nd order polynomials. The combination of these two conditions ensures the optimality of the discretization, as explained and illustrated in Mavriplis (1989).

Using the same choice of basis as in (5) for the functions ϕ and performing the inner products by Gauss-Lobatto quadrature as in (4), the nonconforming discretization incurs in practice only a pre- and post-multiplication of matrices in the usual conforming discrete set of matrix equations. The global Laplace operator can therefore be thought of as a local operator "mortared" together by the new matrix operators, which serve as a new form of the direct stiffness procedure.

The domain decomposition decoupling afforded by this formulation allows for efficient parallel implementation. Furthermore all local structure remains intact despite global irregularity, as in the case of non-propagating mesh refinement. The nonconforming mesh corresponding to the conforming mesh of Figure 1 for the wedge calculation is shown in Figure 2. This mesh has $K = 30$ elements and was used to calculate the flow past the wedge with $N_1 = N_2 = 7$. Note the globally irregular structure and obviously the savings in resolution and hence computational effort.

3. RESULTS

The results we present here correspond to Reynolds number $R = \frac{Q}{\nu} = 1560$, where Q is the imposed flowrate, and ν is the fluid viscosity. Two different approaches in flow visualization have been used for this study: first streamline patterns are computed at several time instances during the time-integration, and secondly the concentration field of a scalar (mimicking the dye visualization experiment of Pullin and Perry) was computed along with the equations of motion. Results from this latter method have been presented in Karniadakis (1989) and exhibit a remarkable resemblance with the photographs taken in the experiment. Here in Figure 3a-c we plot instantaneous streamlines at time $t = 9sec$ for three different wedge-angles (60, 96, and 5 degrees respectively). It is seen that the shape of the primary vortex varies sigificantly as the geometry changes, and is far from the circular shape described by Kaden's (1931) solution. In particular, the innermost spirals are circular with the outer spirals highly distorted confirming the results of Krasny (1987). Furthermore, a tertiary vortex system consisting of relatively large eddies appears in the near-apex wedge region with strength increasing with

the wedge-angle; these counter-rotating eddies appear after a characteristic time δt_v associated with viscous effects. Such a multiple vortex structure represents a region of almost constant vorticity; Pullin and Perry (1980) have observed an identical structure for impulsive flows except for the case of a slender wedge as is also verified by our simulation (Figure 3c).

The horizontal position x_c of the primary growing vortex relative to the wedge-apex is plotted in Figure 4 for a wedge-angle 60 degrees; also included are the experimental data of Pullin and Perry (1980) as well as the inviscid similarity solution given by Pullin (1978). It is seen that our predictions corresponding to the high resolution simulations fall between the experimental data and the analytical solution. In particular, it is shown that given that the similarity theory predicts growth of $x_c \propto t^{5/7}$, the numerical simulation predicts a faster growth. The experimental results are in good agreement for early times, however for time greater than $t = 8sec$ there is a great deviation from both computation and theory; such a discrepancy is justified from the fact that the dye diffuses significantly at later times making the measurement of the vortex center from the still photographs quite inaccurate. The discrepancy between the computed position and the one predicted by the theory should be attributed to the viscous effects; indeed such a discrepancy appears after time $t = t_v$, after which strong secondary eddies (Figure 3) are formed which can displace the center of the vortex and thus modify the dynamics of the evolution of the vortex sheet. As regards the predictions of the nonconforming spectral element simulation it is clear that the wedge-apex region is underresolved with the secondary eddies barely captured (as seen in Figure 5) and thus have no effect on the growth of the large-scale vortex; this perhaps can explain the closer agreement with the results of inviscid theory. Similar results were also obtained by Spalart et al (1984) using vortex methods: in their simulation underresolution of the flow leads to underestimation of x_c even below the inviscid results.

Finally, we address the question of formation of small-scale vortices at the edge of the rolled-up sheet. Such a phenomenon has been consistently photographed for very slender wedges, however, the cause of its appearance has been the subject of controversial explanations (Pullin and Perry (1980)). In Figure 6 we plot the instantaneous streamlines for the flow past the 5° wedge at time $t = 7sec$ after the flow starts. The existence of rather strong wiggles in the streamline pattern is indicative of distributed centers of vorticity concentration. However, one may argue that this is a result of underresolution of flow at the leeward face of the wedge: experimentation with much finer resolution produced identical results. At later times, however, ($t \geq 10sec$) these wiggles disappear and the primary vortex regains a perfectly elliptic shape. The experiments by Pierce (1961) and Pullin and Perry (1980) for the slender wedge have been performed at much higher Reynolds number, so no direct comparison can be made with our calculations; it is expected though that persistence of the transient instability we observe in our simulations will be strongly dependent on the Reynolds number. Such an investigation that addresses stability of the rolled-up shear layer including the effect of external excitation is currently underway.

We would like to thank P. Moin and J. Kim for suggesting this problem to G. Karniadakis as a test for the spectral element method. Most of the calculations presented here were performed on the CRAY-X/MP48 at the Pittsburgh Supercomputing Center.

REFERENCES

[1] Dorr, M., Numer. Mathem. (submitted), 1989.

[2] Kaden, H., Ing. Arch., 2:140, 1931.

[3] Karniadakis, G.E., Appl. Num. Math., to appear.

[4] Krasny, R., J. Fluid Mech., 184:123, 1987.

[5] Maday, Y. and Patera, A.T., State–of–the–Art Surveys in Comput. Mech., 1987.

[6] Mavriplis, C., Ph.D. thesis, M.I.T., 1989.

[7] Pierce, D., J. Fluid Mech., 11:460, 1961.

[8] Pullin, D., Phys. Fluids, 22:219, 1979.

[9] Pullin, D. and Perry, A., J. Fluid Mech., 97:239, 1980.

[10] Prandtl, L. and Tietjens, McGraw–Hill, 1934.

[11] Spalart, P., Leonard, A. and Baganoff, D., TM84328, NASA Ames, 1983.

[12] Strang, G. and Fix, G., Prentice Hall, 1973.

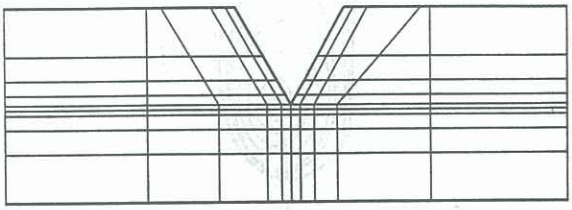

Figure 1: Conforming spectral element mesh; the total number of nodes is 3000

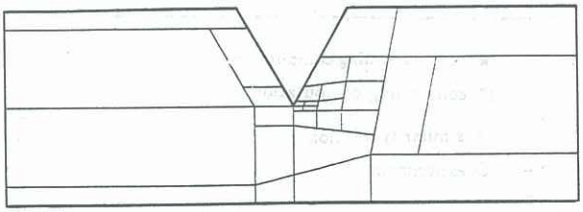

Figure 2: Nonconforming spectral element mesh; the total number of nodes is 1000

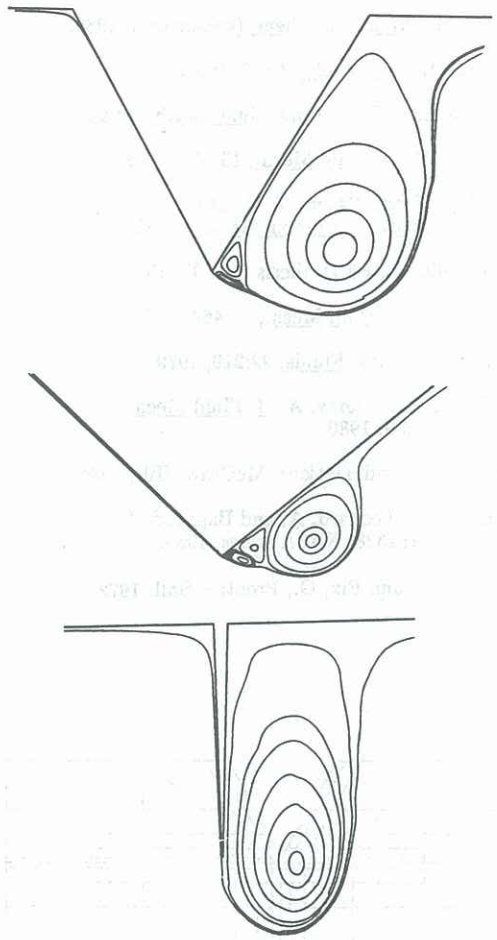

Figure 3: Instantaneous streamlines at time t=9s wedge angle (a) 60°; (b) 96°; (c) 5°

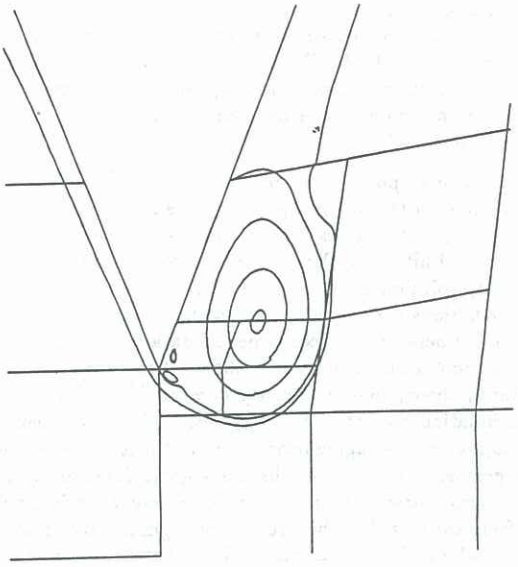

Figure 5: Instantaneous streamline patterns near the wedge tip based on nonconforming spectral element simulations at time t = 5s (wedge–angle 60°)

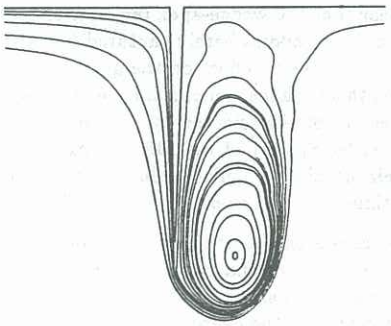

Figure 6: Sudden appearance of wiggles in the rolled–up shear layer indicative of a transient instability (wedge–angle 5°)

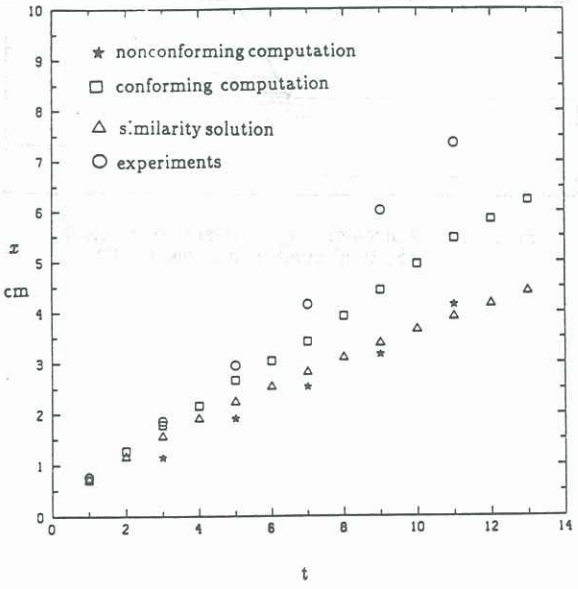

Figure 4: Horizontal position of the primary growing vortex relative to the wedge–apex (wedge–angle 60°)